

Transit Detectability of Ring Systems Around Extrasolar Giant Planets

Jason W. Barnes and Jonathan J. Fortney¹

Department of Planetary Sciences

University of Arizona

Tucson, AZ 85721

`jbarnes@c3po.barnesos.net, jfortney@arc.nasa.gov`

ABSTRACT

We investigate whether rings around extrasolar planets could be detected from those planets' transit lightcurves. To this end we develop a basic theoretical framework for calculating and interpreting the lightcurves of ringed planet transits based on the existing framework used for stellar occultations, a technique which has been effective for discovering and probing ring systems in the solar system. We find that the detectability of large, Saturn-like ring systems is largest during ingress and egress, and that reasonable photometric precisions of $\sim 1 - 3 \times 10^{-4}$ with 15-minute time resolution should be sufficient to discover such ring systems. For some ring particle sizes, diffraction around individual particles leads to a detectable level of forward-scattering that can be used to measure modal ring particle diameters. An initial census of large ring systems can be carried out using high-precision follow-up observations of detected transits and by the upcoming NASA *Kepler* mission. The distribution of ring systems as a function of stellar age and as a function of planetary semimajor axis will provide empirical evidence to help constrain how rings form and how long rings last.

Subject headings: occultations — planets: rings — planets and satellites: individual (HD209458b) — techniques: photometric

1. INTRODUCTION

Present understanding of extrasolar planets resembles that of solar system planets when Galileo first used the telescope for astronomy in 1610. He discovered that the planets of our solar system variously display disks, phases, moons, and ring systems (Galilei 1989). Though the planets he was studying had been known for thousands of years, before Galileo's telescopic observations scientists knew only the character of their motions and lacked a method for learning more. Now that the orbital parameters for 120 planets orbiting other stars are available, we are looking for the breakthrough techniques that will lead us to the next level of understanding for these new extrasolar planets, just as Galileo's telescope did 400 years ago for the planets known in ancient times.

We think that the most promising technique for characterizing extrasolar giant planets in the near future is precision photometry.

Photometric monitoring of stars has resolved one transiting planet detected by radial velocity methods, HD209458b (Charbonneau et al. 2000; Henry et al. 2000), and three more detected by ground-based transit surveys: OGLE-TR-56b (Konacki et al. 2003), OGLE-TR-113b (Bouchy et al. 2004; Konacki et al. 2004), and OGLE-TR-132b (Bouchy et al. 2004). Fitting the transit lightcurve of HD209458b allowed Brown et al. (2001) to measure the

size of the planet's disk, which determined HD209458b to be a gas giant like Jupiter. Further observations of the wavelength dependence of HD209458b's transit lightcurve revealed the presence of upper atmospheric sodium (Charbonneau et al. 2002) and an extensive hydrogen envelope (Vidal-Madjar et al. 2003).

Extrasolar planets in orbits not in the plane of the sky (*i.e.*, not face-on) should show phases. Though searches to date have not detected the photometric signature expected for the phases of orbiting extrasolar planets, these studies were able to place constraints on the reflective properties of close-in giant planets (Charbonneau et al. 1999; Collier Cameron et al. 2000, 2002).

Sartoretti & Schneider (1999) showed that large moons around transiting extrasolar planets should reveal themselves both by additional stellar dimming while they transit and by their effect on the transit timing of their parent planets. Using transit photometry from the *Hubble Space Telescope*, Brown et al. (2001) employed this technique to search for moons orbiting HD209458b, but found no evidence for any, consistent with theory for the orbital evolution of such moons (Barnes & O'Brien 2002).

The purpose of the present work is to predict what observational photometric transit signatures a ringed planet might make and to point out the possible scientific value of a survey for such signatures. It is not intended to be a final or comprehensive theory for the study of extrasolar rings in transit. It is intended to serve as a guide for observers, so that they might have insight into what the unusual deviations in their transit lightcurve residuals might be.

¹Now at NASA Ames Research Center, Mail Stop 245-3, Moffett Field, CA 94035

In this paper, we first investigate the possible science that could be done from a transit photometric ring survey. Next we study the practicality of detecting systems of rings around extrasolar giant planets using transit photometry by looking into the effects of extinction and diffraction. Lastly, we simulate a transit of Saturn as a well-known example.

2. MOTIVATION

2.1. Rings in the Solar System

Ring systems orbit each of the giant planets in our solar system. The rings are made up of individual particles orbiting prograde in their host planet's equatorial plane. However, each system of rings is unique, differing in character, radial and azimuthal extent, optical depth, composition, albedo, and particle size. See Table 1 for a brief summary of what is known about the rings of our solar system.

Among solar system planets, by virtue of its rings' large effective cross-sectional area (which we define to be the product of the rings' actual cross-sectional area and one minus their transmittance) Saturn by far has the greatest capability to block starlight during a transit. Thus for the remainder of this paper we will concentrate on ring systems with similar radial extent and optical depth, which we refer to as Saturn-like ring systems. The ring systems of Uranus, Neptune, and Jupiter would remain undetectable with current or predicted future photometric capabilities, and thus our analysis is only applicable to the aforementioned large, Saturn-like ring systems.

2.2. Rings in Extrasolar Systems

A survey of ring systems orbiting extrasolar giant planets can potentially address the two big picture questions about ring systems: (1) how do rings form? and (2) how long do rings last?

If Saturn's ring system formed recently and ring systems decay quickly, then extrasolar ring systems as spectacular as Saturn's should be rare. If ring systems around extrasolar giant planets are shown to be common, then ring systems are either long-lived, easily and frequently formed, or both.

The typical lifetime of ring systems can be tested directly based on the distribution of ring systems detected around stars of differing ages. If ring systems survive for many billions of years, then the frequency of ring systems as a function of stellar age should be either flat (if rings are primordial) or increasing (if they are formed by later disruptive events). If rings are less prevalent around planets orbiting older stars, then typical ring lifetimes can be constrained by the observations.

Uncertainties in stellar age measurements are notoriously large, though, and those uncertainties will propagate into any subsequent estimate of ring formation times and

lifetimes using our method. It seems reasonable that 10 - 20 ringed planets would be necessary to attempt this type of analysis – a number possibly in excess of the number of ringed planets *Kepler* alone will discover, depending on what fraction of planets have Saturn-like ring systems. On the other hand, *Kepler* might discover that a large fraction of very young (< 1 Gyr) planets have ring systems, thus improving the statistics and revealing a primordially created population of rings. At present we lack the basic understanding that would be required to create a model to predict the statistics for ring distribution as a function of stellar age.

Photometry during stellar occultations revealed the Uranian and Neptunian ring systems; photometry of extrasolar giant planet transits can be used to search those planets for rings. Note, though, that an extrasolar ring census could also be done using photometry of reflected light from directly detected planets (Dyudina et al. 2003; Arnold & Schneider 2004) or by microlensing (Gaudi et al. 2003).

Planets with small semimajor axes are most likely to transit. However, ring systems around the closest-in planets (semimajor axis less than ~ 0.1 AU) are expected to decay over timescales that are short compared with the age of the solar system, due to such effects as Poynting-Robertson drag and viscous drag from the planet's exosphere (Gaudi et al. 2003). Although the currently ongoing transit searches are aimed at finding only these short-period planets (Horne 2003), the *Kepler* (see Jenkins & Doyle 2003, and references therein) space mission will monitor a single region of the sky for up to 4 years and be capable of detecting transiting planets with any period.

Planets with periods greater than the length of a photometric survey cannot have their periods determined, and thus cannot be followed up on. As we show in this paper, though, the *Kepler* mission should attain sufficient temporal resolution and photometric precision to detect Saturn-like ring systems without additional observations. The number of transiting planets at 10 AU that we expect to be detected is low. Using the approximate detection probability $R_*/a_p \times 2/\pi \times T_{\text{obs}}/P_{\text{planet}}$ (with R_* as the stellar radius and a_p the planet's semimajor axis) for planets with periods (P_{planet}) longer than the observation time (T_{obs}), if every star had a Saturn then *Kepler* would find ~ 5 among the 100,000 stars it will monitor. If all Saturn-like ring systems are made of water ice, then only transiting planets at large semimajor axes could possess rings and therefore the statistics for a ring survey of extrasolar giant planets are not good.

However, every large ring system need not necessarily be made of water ice. Although the composition and temperature of Saturn's rings may yet prove necessary for their formation and continued existence, we cannot at present rule out silicate rings inward of the ice line, metallic rings around close-in planets, or rings made of lower temperature ices at larger planetary semimajor axes. *Kepler* will find and search 50 HD28185b-type giant planets at 1AU, if every star has one. The presence or absence of these

TABLE 1
CHARACTERISTICS OF KNOWN RING SYSTEMS

Planet	Ring Particle Size	Ring Composition	Ring System Age	Ring Origin
Saturn	0.01-10 m	water ice	young?	unknown
Uranus	not yet measured	uncertain	unknown	unknown
Neptune	not yet measured	uncertain	unknown	unknown
Jupiter	mostly < 1 μ m	silicate dust	continuously replenished	hypervelocity impacts into adjacent moonlets

unfamiliar ring systems will help constrain the processes involved in the formation and evolution of ring systems as a whole.

3. EXTINCTION

3.1. Methods

Rings affect a planet’s transit lightcurve in two ways: extinction and scattering. Multiple scattering is negligible in most cases. Extinction occurs as a result of the interception of incoming starlight by ring particles that either absorb, reflect, or diffract the light, removing it from the beam. The amount of light transmitted through any given portion of the ring is equal to $e^{-\tau/\beta}$ where τ is the normal optical depth and β is equal to the sine of the apparent tilt of the rings (zero being edge-on). The factor β compensates for the increased extinction at low tilt angles.

No presently existing or near-future technology can resolve other main-sequence stars, much less a planet in transit across a star’s disk. Instead, we calculate the total stellar brightness that would be observed during the transit, and determine whether the structure of dimming expected for transiting planets with rings could be differentiated from the structure expected for planets without rings.

To determine the amount of expected dimming, we compare the integrated stellar surface brightness to the flux intercepted by a planet and its potential ring system. The stellar surface brightness I as a function of projected distance from the star’s center, ρ , is expressed in terms of $\mu = \cos(\sin^{-1}(\rho/R_*)$) as in Barnes & Fortney (2003), where c_1 and c_2 are coefficients that parameterize limb darkening:

$$\frac{I(\mu)}{I(1)} = 1 - c_1 \frac{(1-\mu)(2-\mu)}{2} + c_2 \frac{(1-\mu)\mu}{2}. \quad (1)$$

The constants c_1 and c_2 define the character of the limb darkening, with c_1 measuring the overall magnitude and c_2 the second order shape. This nontraditional limb darkening parameterization allows meaningful representation of stellar limb darkening from a single parameter, c_1 , instead of two or more (see also Brown et al. 2001, Section 3; our c_1 corresponds to their $u_1 + u_2$) and is therefore more appropriate for use in fitting transit lightcurves.

We calculate the total stellar flux (F_0) by integrating $I(\mu)$ across the disk of the star over the projected distance from the star’s center, ρ :

$$F_0 = \int_0^{R_*} \frac{2\pi\rho I(\rho)}{(R')^2} d\rho. \quad (2)$$

The distance from the star to the observer, R' , drops out in Equation 4 and so is not calculated explicitly.

To determine the fraction of starlight blocked by the planet or intercepted by ring material, we integrate over both ρ and the apparent position angle θ :

$$F_{blocked} = \int_0^{R_*} \int_0^{2\pi} \frac{I(\rho) (1 - T(\rho, \theta))}{(R')^2} \rho d\theta d\rho, \quad (3)$$

where $T(\rho, \theta)$ is the fraction of light transmitted at the corresponding ρ, θ location. The relative flux detected by an observer at time t is then

$$F(t) = \frac{F_0 - F_{blocked}}{F_0}. \quad (4)$$

This algorithm is similar to the one that we used in Barnes & Fortney (2003), but with an explicit azimuthal integral to incorporate ring effects.

As we demonstrated in Barnes & Fortney (2003), the difference between the transit lightcurve of a given planet and the lightcurve of *that same planet* with an additional feature (such as rings or oblateness) is not an appropriate measure of the detectability of the feature. Because the parameters of the transit such as the planet radius (R_p), stellar radius (R_*), impact parameter ($b = \rho_{\min}/R_*$), and stellar limb darkening (c_1) are initially unknown and must be determined using a fitting process, the presence of the ring manifests itself as an astrophysical source of systematic error in the measurement of these quantities. These errors act to simulate the transit of the ringed planet, and thus diminish the ring detectability. We then define the detectability of a ring around a transiting planet to be equal to the difference between the ringed planet’s transit lightcurve and the lightcurve of the planet-only model that best fits the ringed planet’s lightcurve.

3.2. Results

Figures 1 and 2 show the expected detectability (in extinction only) of a planetary ring. In these figures, we sim-

ulated transits of a spherical $1R_{Jup}$ planet with a $\tau = 1.0$ ring in its equatorial plane extending from $1.5R_{Jup}$ to $2.0R_{Jup}$ in order to show the character that the detectability of rings might have. We address more realistic ring systems in Section 5. Although the particular lightcurves shown are for a planet with a semimajor axis of 1.0 AU, *the detectability for planets at other distances from their stars is the same*, differing only in the timescale. Thus, the results in this section apply equally well for transiting planets that orbit their stars at 10AU and for close-in planets. For a $1M_{\odot}$ star, to obtain the detectability curve of a planet with semimajor axis a_p multiply the values on the time axis by a factor of $\sqrt{a_p/1.0\text{AU}}$. Transits of planets with differing radii and ring structures will differ quantitatively from those plotted in Figures 1 and 2.

For each case, the extinction of starlight through the rings leads to a deeper transit, and therefore a transit lightcurve’s best-fit ringless model planet is larger than the real planet. If an observer were to use the transit depth to estimate the planet’s parameters, he or she would overestimate the planet’s radius. This could account for the anomalously high radius of HD209458b (e.g., Bodenheimer et al. 2003). However, we find this explanation unlikely: rings around HD209458b would be subject to strong orbital perturbations due to their proximity to the star (Gaudi et al. 2003), and any ring system would be in the planet’s equatorial plane and therefore be seen edge-on during transit if, as expected, the planet is in tidal equilibrium.

We introduce an angle ϕ , which we call the axis angle, to represent the azimuthal angle around the orbit normal corresponding to the direction that the planet’s rotational angular momentum vector points (see Figure 3). We measure ϕ from the direction that the planet is travelling in at mid-transit and positive is defined to be toward the star. The axis angle thus corresponds to the planet’s season at midtransit, with $\phi = 0$ being the northern fall equinox, $\phi = \pi/2$ being the northern summer solstice, $\phi = \pi$ being the northern spring equinox, and $\phi = 3\pi/2$ being the northern winter solstice.

We assume the rings to be two dimensional, which is quite a good approximation for the rings of Saturn, Uranus, and Neptune: Uranus’ rings, for instance, are only 1 m thick (Karkoschka 2001). Hence, the rings we model do not at all contribute to the lightcurve if they are edge-on during transit, and thus the detectability for planets with obliquity (q) near 0° or with axis angle (ϕ) near 0 or π is negligible. Also, due to the geometry of the problem, transits for a given axis angle and its opposite are identical. Hence, the transits of planets at solstice, such as those in Figure 1, could have either $\phi = \pi/2$ or $\phi = -\pi/2 = 3\pi/2$.

In the symmetric case ($\phi = \pi/2$; Figure 1), for low impact parameter transits ($b = 0.2$, upper subgraph) the lightcurve of the ringed planet starts earlier than that of that transit’s best-fit spherical planet as the rings encounter the stellar limb first, leading to an initial downturn in the detectability curve. That curve turns around when the best-fit naked planet hits and the ring’s inner gap en-

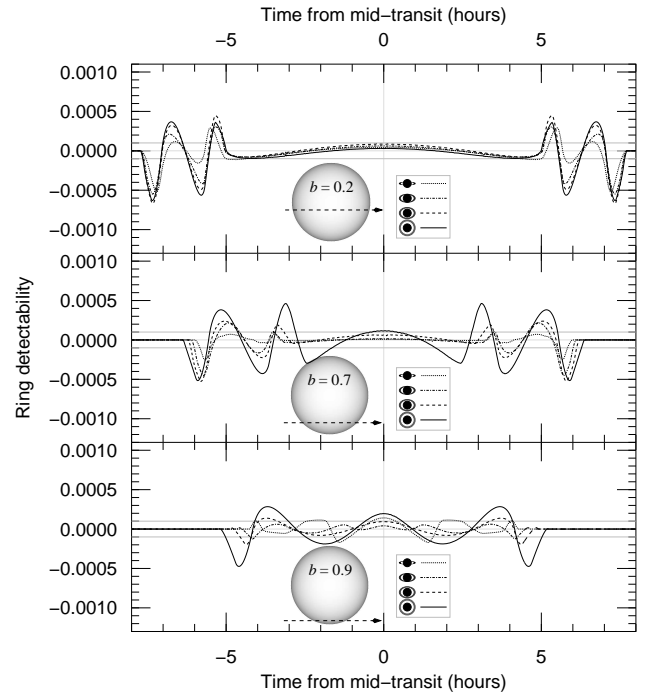


Fig. 1.— Detectability of extinction through symmetric planetary rings in transit, defined as the difference between the transit lightcurve of the given ringed planet and its best-fit spherical planet model. This graph shows the detectabilities for rings tilted directly toward the observer, Figure 2 shows the detectability for asymmetric geometries. Each subgraph shows the detectability for planets of four different obliquities, 10° (dotted line), 30° (dash-dot line), 45° (dashed line), and 90° (solid line; face on) for simulated transits with impact parameter 0.2 (upper), 0.7 (middle), and 0.9 (lower). The signal is greater than the typical noise limit for both Kepler and the HST HD209458b observations, 1×10^{-4} (gray lines), but is very localized in time to the regions surrounding ingress and egress. Both high photometric precision and high temporal resolution would be necessary to detect the ring signal.

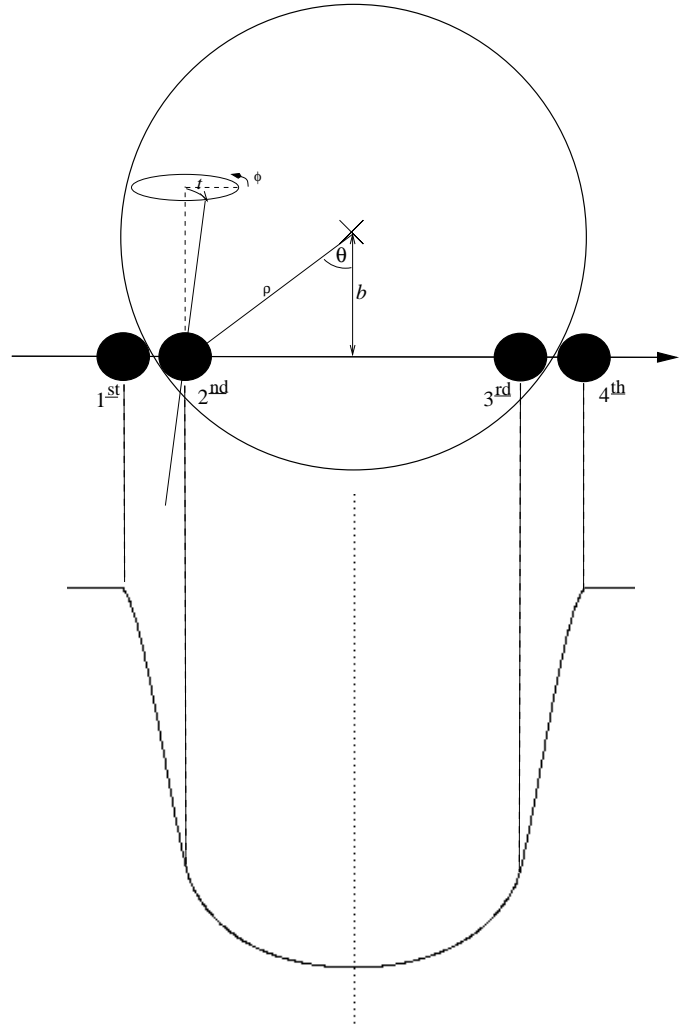
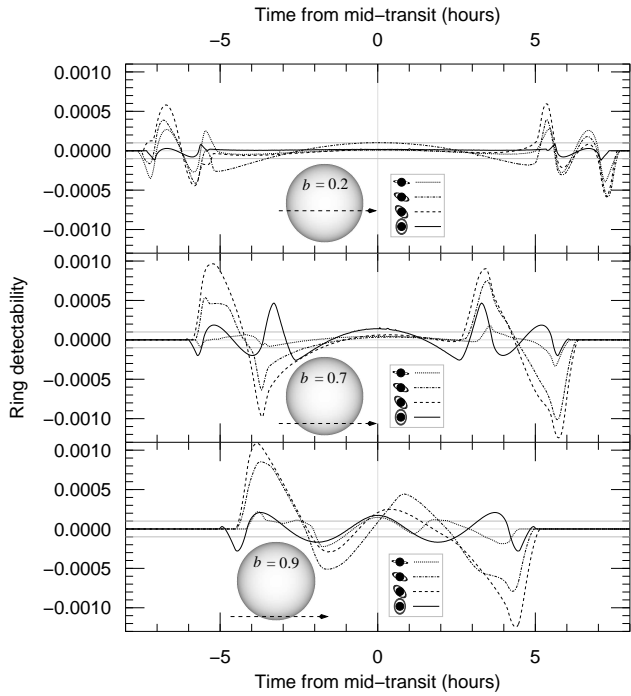


Fig. 3.— Schematic of transit geometry and variable definitions.

Fig. 2.— Detectability of extinction through asymmetric planetary rings in transit, defined as the difference between the transit lightcurve of the given ringed planet and its best-fit spherical planet model. This graph shows the detectabilities for rings tilted in a direction such as to maximize their transit detectability, so the axis angle ϕ is set to $\pi/4$. Figure 1 shows the detectability for symmetric geometries. Each subgraph shows the detectability for planets of four different obliquities, 10° (dotted line), 30° (dash-dot line), 45° (dashed line), and 90° (solid line; face on) for simulated transits with impact parameter 0.2 (upper), 0.7 (middle), and 0.9 (lower). The signal is greater than the typical noise limit for both Kepler and the HST HD209458b observations, 1×10^{-4} (gray lines). The asymmetric signal is greater than that in the symmetric case, but only by a factor of ~ 2 .

counter the stellar limb at nearly the same time causing a sharp change in derivative, whereby the best-fit lightcurve starts to overtake the ringed planet in total light blocked. As a large fraction of ringed planet itself starts to occult the star, the two hypothetical transits become equal about midway through their ingresses. This trend continues past the midpoint until the inner gap once again causes the simulated ringed planet transit to brighten relative to its best-fit model, and by the end of ingress the edge of the ring encounters the limb of the star at second contact. The bottom of the transit is nearly flat, as both the planets block the same fraction of starlight. This process repeats itself in reverse upon egress.

All things being equal, a non-ringed planet would have a much shorter ingress and shallower transit depth than its ringed twin. But all things are not equal. What happens instead is that the best-fit naked spherical planet model mimics the simulated ringed planet’s lightcurve by lengthening the model fit’s ingress and increasing the model’s transit depth. The resulting fits have a higher impact parameter (b) and greater stellar radius (R_*), which both act to increase the time that the model planet takes to cross the star’s limb. At the same time, the model planet’s radius (R_p) is higher than that of the actual planet to account for the greater effective cross-sectional area that the rings provide the ringed planet. The stellar limb darkening coefficient (c_1) differs only slightly in this case to compensate for the different transit impact parameters, and its inability to completely do so results in the downward bow of the detectability curve through the transit bottom.

At this low impact parameter, the most important distinction between the ringed planet transit and its best-fit model is the ringed planet’s longer ingress, or earlier first contact and later second contact. Because a planet’s rings extend equally far from the planet’s center regardless of obliquity, low obliquity rings ($q \sim 10^\circ$) are as detectable as high obliquity rings ($q > \sim 30^\circ$), but remain distinctive by their smaller central clearing. Though the ingress only lasts about 45 minutes for a planet with HD209458b’s semi-major axis, a planet at 1 AU would have a more leisurely (and more easily sampled) 3.75 hour ingress.

The signature of a symmetric ringed planet is similar to, but distinct from, the detectability signature of a highly oblate planet (Barnes & Fortney 2003). The signature for a symmetric ringed planet returns to zero three times during ingress, while the oblate planet detectability signature returns to zero just twice. The difference between the two is caused by the interior clear area between the planet at the inner edge of the ring. A planet with rings that extend all the way down to the top of the atmosphere would be very difficult to distinguish from a very highly oblate planet by observational means.

At moderate impact parameters (*i.e.*, $b = 0.7$; Figure 1, middle subgraph), expected ring detectabilities are similar in character and magnitude to those at low impact parameter, but last longer due to longer ingress and egress times. However, symmetric, low obliquity ringed planets no longer have such extended ingress times rela-

tive to a ringless planet, and thus have significantly lower detectabilities than they do at lower impact parameters.

High impact parameter symmetric transits of ringed planets (*i.e.*, $b = 0.9$; Figure 1, bottom subgraph) deviate from the patterns described above. Planets with high obliquity have their ring systems extend beyond the star’s edge throughout the transit, and thus become grazing. Lower obliquity planets transiting at high impact parameter have their first contact start no earlier than that of a ringless planet, and thus their detectabilities are less than expected noise levels.

When a ringed planet is not tilted directly toward or away from the observer, the lightcurve that results when the planet transits its star is asymmetric. The asymmetry is greatest for planets in mid-season, those with $\phi = \pi/4 + n\pi/2$ where n is any integer, and the predicted detectability of rings around these planets is displayed in Figure 2. Differences from the symmetric case come about due both to differing lengths of ingress and egress times and to a different part of the planet-ring system making first contact with the stellar limb. These effects are most important when the planet’s projected equatorial plane (*i.e.* the line containing the planet center and the apparent furthest edges of the rings) is parallel to the stellar limb during ingress of egress.

At low impact parameter ($b = 0.2$; Figure 2, top subgraph), the planet’s direction of motion is nearly perpendicular to the stellar limb, and thus the differences between the symmetric and asymmetric lightcurves are small, changing primarily the intensity of the positive and negative deviations but not their character. Small to moderate planetary obliquities ($10^\circ < q < 60^\circ$) therefore have transit lightcurves that strongly resemble the lightcurves from the symmetric case. The least detectable configuration at low impact parameter in the mid-season case is for planets with obliquity $q = 90^\circ$. These Uranus-like objects have symmetric transit lightcurves for all impact parameters, and low detectabilities at $b = 0.2$ because the stellar limb is covered by the rings at the same time the rings’ parent planet is covering the limb (a situation that the best-fit nonringed planet simulates well).

Differences between the time required for ingress relative to the time for egress dominate the lightcurves for planets transiting near the critical impact parameter ($b = 0.7$; Figure 2, middle subgraph). The most detectable cases are those where the projected equatorial plane is parallel to the limb: the $q = 30^\circ$ and $q = 45^\circ$ cases in Figure 2. For these ringed planets, first contact occurs after, and second contact occurs before, the contacts for their best-fit ringless counterparts in the case where the apparent planet motion is left to right (see diagram at upper left of subfigures of Figure 2). Upon egress from transit, the rings encounter the stellar limb before the best-fit spherical planet, and hang on to the limb after the best-fit ringless planet ends its transit. These differences in limb-crossing time result in a large initially positive detectability (ringed minus best-fit nonringed) as the best-fit planet starts its transit before the ringed planet, a transition to negative values while both

are near second contact, and then a return to near-zero detectability for the transit bottom when both objects are entirely in transit. On egress, the resulting detectability is again initially positive as the ringed planet lightcurve brightens when the rings exit transit before the limb of the best-fit planet, and again becomes negative when the best-fit planet exits transit before the lingering final edge of the rings of the ringed planet. This character of transit lightcurve is appropriate for planets with $-\pi/2 < \phi < \pi/2$. For planets with $\pi/2 < \phi < 3\pi/2$ the sequence would be time-reversed. For low obliquity ringed planets transiting at $b = 0.7$, the asymmetric component of the transit lightcurve is overshadowed by the symmetric component, and thus in character resembles a cross between the two. At maximum obliquity ($q = 90^\circ$), the detectability curve is symmetric but moderately large, with maxima resembling the $\phi = 0$ case in magnitude.

The detectabilities of asymmetric ringed planets when transiting at high impact parameters ($b = 0.9$; Figure 2, bottom subgraph) are similar to those for $b = 0.7$, except that the transit lightcurve sequences are truncated due to the grazing nature of this particular transit. Because there is no second or third contact, there is no transit bottom and the detectabilities never return to near zero as they do in the non-grazing cases.

The Discovery mission *Kepler*, with typical photometric precision 1×10^{-4} and 15 minute sampling (Jenkins & Doyle 2003) should be most sensitive to planets with large ring systems and with periods longer than ~ 1 yr, irrespective of scattering (see Section 4). Higher cadence measurements with similar precision, as acquired by *HST* (Brown et al. 2001) and as may be possible in the near future from the ground (Howell et al. 2003), would be capable of detecting rings around closer-in planets, if such rings exist (see Section 2).

4. DIFFRACTION

4.1. Theory

Calculation of scattering from a transiting extrasolar ring system resembles the calculation of scattering from a ring in the solar system as it occults a star. In both problems, starlight passes through a thin slab of ring particles and is altered on its way to the observer, who measures the star's brightness. However, while for solar system applications the distance between observer and ring is small and the observer-star and ring-star distances are both large, in the transit case the distance between the ring and the star is small and the observer-star and observer-ring distances are large. French & Nicholson (2000) analyzed photometry from Saturn's occultation of the star 28Sgr in 1989, and we base our theoretical models on theirs, with appropriate modifications for the altered circumstances between occultations and transits.

Particles between 1mm and 10m in size contribute most of the opacity in the rings around Saturn, Uranus, and Neptune (French & Nicholson 2000; Cuzzi 1985; Ferrari &

Brahic 1994). Particles like these, much larger than the wavelength of light passing through them, scatter light in the forward direction when incident light diffracts around individual particles. The relative scattered flux as a function of the scattering angle, the phase function $P(\theta)$, is (assuming spherical particles; French & Nicholson 2000)

$$P(\theta) = \frac{1}{\pi} \left(\frac{J_1\left(\frac{2\pi a}{\lambda} \sin \theta\right)}{\sin \theta} \right)^2, \quad (5)$$

where a is the particle radius, λ is the wavelength of light, and the function $J_1()$ represents the first Bessel function. Equation 5 integrates to 1.0 over the forward 2π steradians in order to conserve flux, but is only accurate when $\theta \ll 2\pi$. The shape of this function resembles that of a stellar diffraction point spread function from a telescope. In effect, it represents the collective Poisson's spots of the ring particles viewed from, say, 50 parsecs away.

The total flux diffracted by the ring particles is equal to the flux that they intercept. This can be inferred from Babinet's Principle: the diffraction of a beam caused by a particular screen containing both transparent and opaque areas appears the same as the diffraction of the screen's inverse, which has the opaque and transparent areas switched (see, e.g., Hecht 1998, the phase of the diffracted light is opposite in each case). Hence the flux of light diffracted by a ring filled with particles of radius a is the same as the flux of diffracted light coming from a black sheet peppered with holes of radius a , which is equal to the light transmitted through the holes in the sheet. Thus on top of absorption, diffraction provides an additional, equal source of opacity for photons travelling straight through the ring. This effect can be confusing (Cuzzi 1985), so we follow French & Nicholson (2000) in explicitly representing the optical depth resulting from geometrically intercepted, absorbed light as τ_g and the total optical depth, including scattering effects, as $\tau = 2\tau_g$.

The actual effective geometrical cross-sectional area of the ring particles varies with optical depth due to shadowing effects. We express the total scattered flux that emerges from a point on the ring integrated over all angles (F_{sc}^R) as a function of the flux incident on that point (F_i) (French & Nicholson 2000):

$$\frac{F_{sc}^R}{F_i} = \frac{\tau_g}{\beta} e^{-2\tau_g/\beta}. \quad (6)$$

F_{sc}^R peaks at $\tau = 1$ with a value $(2e)^{-1}$. The variable β is equal to the sine of the apparent tilt of the rings (zero being edge-on), and compensates for the correspondingly higher optical depths for low tilt. The flux exiting the ring in the direction of the observer (designated \oplus) at a specific angle (θ) when diffracted from a *point source star*, F_{sc}^\oplus , is the product of the total scattered flux and the phase function, where θ corresponds to the angle between the point source star-ring particle line and the line of sight (French & Nicholson 2000):

$$F_{sc}^\oplus(\theta) = F_{sc}^R P(\theta) \quad (7)$$

In the occultation case, the star behaves as a point source when viewed from both Earth and the ring. However, for transits the planet is in close enough proximity to the star that the star must be treated as an extended source. Hence, the scattered flux from a point on the ring is not simply the product of the incident flux on the ring and the phase function, as in the solar system case, because θ is not constant. Instead we integrate over the stellar disk to derive the total scattered flux at Earth from across the extended star, ${}^\circ F_{sc}^\oplus$.

We first calculate the illumination provided for each parcel of the star onto the ring. To determine this incident flux, we treat the star as a limb-darkened lambertian disk. The flux incident on a point in the rings from a region of that disk depends on the emergent stellar flux from the region as a function of the projected distance from the star's center, $F_*(\rho)$ (which we get from Equation 1); the area of the region, E ; and the distance between the region and the ring portion in question, which we approximate to always be a_p , the planet's semimajor axis:

$$F_i(R, \rho, \phi) = F_*(\rho) \frac{E \cos^2(\theta(R, \rho, \phi))}{\pi a_p^2}. \quad (8)$$

One of the two $\cos \theta$ terms derives from our assumption that the star is a flat disk, and the other comes from the need to measure the incoming flux in a plane perpendicular to the observer's line of sight. Though the second $\cos \theta$ is real, the first term is an artifact of our model, and as such is probably not representative of an actual planet around a spherical star. However, in the transit situation θ is small and the extra $\cos \theta$ does not inflict a significant adverse effect on the resulting calculation.

To obtain the total scattered flux from the extended star, we integrate the scattered flux for a point source, Equation 7, over the projected distance from the star's center (ρ) and the azimuthal angle (ϕ), using Equation 8 for the incident flux F_i . The total flux emergent from the ring, scattered from the extended star in the direction of the observer (${}^\circ F_{sc}^\oplus(R)$), comes from integrating the star's flux over each infinitesimal area of the star $E = \rho d\phi d\rho$, times the phase function for the particular angle θ between that area, the scatterer, and the observer:

$${}^\circ F_{sc}^\oplus(R) = \int_0^{R_*} \int_0^{2\pi} F_{sc}^R(\rho, \theta) P(\theta(R, \rho, \phi)) \rho d\phi d\rho. \quad (9)$$

Due to circular symmetry around the center point of the limb darkened star, the *total* integrated incident flux is only a function of the projected distance of the ring from the star's center, R , and not of the azimuthal location of the rings around the star, ϕ . When incorporating scattered light into the calculation of transit lightcurves, we integrate Equation 9 numerically using an adaptive stepsize Runge-Kutta algorithm from Press et al. (1992).

4.2. Results

We show the relative contribution of diffracted light through a cloud of same-size particles in Figures 4 and

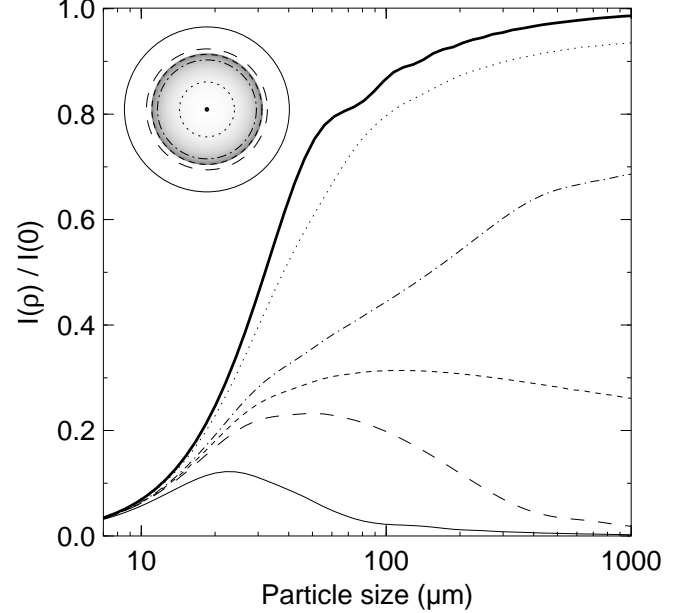


Fig. 4.— This plot shows scattering effectiveness as a function of particle size at $0.5\mu\text{m}$ for hypothetical parcels of ring particles located 1 AU from the star but at varying projected distances from the star's center. We used a stellar diameter of $1.0R_\odot$ and limb darkening coefficient c_1 equal to 0.64 (similar to the measured value for HD209458); the limb darkening in the inset graphic is true. We plot for the projected distances depicted in the graphic inset in the upper left: $\rho = 0.0R_*$ (thick solid line), $\rho = 0.5R_*$ (dotted line), $\rho = 0.9R_*$ (dot-dashed line), $\rho = 1.0R_*$ (short-dashed line), $\rho = 1.1R_*$ (long-dashed line), and $\rho = 1.5R_*$ (thin solid line). We have not included the effects of optical depth on the amount of light scattered – to get the actual expected scattered flux multiply the values in this graph by the τ -factor, the right side of Equation 6. At low particle diameters, the scattering effectiveness approaches a constant and diminishing value for all projected stellar distances. For high particle diameters, the effectiveness approaches the relative flux of the point on the star directly behind the cloud of particles – zero for points off the limb of the star, and following the limb darkening while inside the limb. For particle diameters near the critical particle diameter a_{crit} (see Equation 10; a_{crit} for the conditions used to generate this graph is $70\mu\text{m}$), the brightness for clouds of ring particles sitting just off the star's limb is maximized.

5. The amount of refracted light per unit projected area relative to the flux per unit area at the star’s apparent center is plotted as a function of particle size for differing projected distance from the star center (Figure 4), and as a function of projected distance from the star center for differing particle sizes (Figure 5). For each we assume the planet’s semimajor axis is 1.0 AU and that its parent star has a radius of 1 R_{\odot} with limb darkening coefficient c_1 equal to 0.64 ($(u_1 + u_2)$) as measured by Brown et al. (2001) for HD209458b) for the star. The optical depth factor from Equation 6 is not included – to obtain ${}^{\circ}F_{sc}^{\oplus}$ for any particular optical depth multiply the values on the graph by the right side of Equation 6 .

In the limit of very large particle sizes (~ 0.1 mm or larger for the 1 AU case), the angles by which light is diffracted around particles becomes very small. These very large particles diffract the light only from the point directly behind them on the star toward the observer, and therefore in the large particle limit the maximum diffracted flux per unit area at a given point is equal to the flux emitted by the star at the point behind the ring (times the optical depth factor). Hence to the rightward edge of Figure 4 the scattered fluxes approach the flux levels at the equivalent point on the stellar disk. In Figure 5, the flux scattered by a sufficiently large particle would trace the limb darkening of the star for $\rho < 0.5D_*$ and be zero for all values larger than $0.5D_*$, similar to the curve of the 1 mm particles plotted.

For a transiting ring made up of large particles, diffraction does not affect the shape of the lightcurve. However because light diffracted out of the incident beam is redirected to the observer, diffraction would act to partially fill in the lightcurve during the transit, reducing the total transit depth (Figure 6). The reduced depth gives the impression that the rings are dispersing less flux than they really are. Thus, if the ring particles are large, the *measured* optical depth of the rings is equal to the geometrical optical depth, $\tau_g = \tau/2$, because the light diffracted out of the beam is entirely replaced (the same as if there were no diffraction at all).

For small particles (smaller than $\sim 10\mu\text{m}$ for the 1 AU case), incoming light is diffracted nearly isotropically. In this limit only a small fraction of the incident flux is diffracted in any one direction, and the received scattered flux is constant over the planet’s orbit (except, of course, during the secondary eclipse). The diffracting behavior of such particles is represented by the leftmost edge of Figure 4 and resembles the behavior of the $10\mu\text{m}$ particle in Figure 5.

Since for a ring made up of small particles the diffracted flux reaching the observer is unvarying, the shape of the planet’s transit lightcurve is the same as it would be in the absence of scattering (Figure 6). For this case the best-fit measurement of the ring’s optical depth would represent the total optical depth, $\tau = 2\tau_g$: a negligible fraction of the diffracted light reenters the beam.

Note that the large particle and small particle cases

cannot be distinguished based on their transit lightcurves alone. If a ring were detected in transit, but no distinctive signature of scattering was found (like are described below), it would be impossible to determine whether the ring’s component particles were large or small. Likewise the proper interpretation of the measured optical depth would also be degenerate.

For ring particles that lie in between these extremes of size, scattering affects the lightcurve and can be used to infer the size of the component particles that make up the ring. In this moderate regime, the light diffracted toward the observer from a parcel of ring particles comes from a circularly symmetric region behind the parcel that grows in size as the particles’ diameters shrink. This footprint, shown in Figure 7, represents a weighted map of where photons scattered toward the observer come from. Most of the light comes from the area within the first fringe.

The effect of scattering on a transit lightcurve is maximized for ring particles near the size that has its first diffraction fringe a projected distance R_* from the particles. This critical particle size is large enough to allow the footprint to scatter a lot of light toward the observer while the ring is in front of the star’s disk, but small enough to scatter significant light toward the observer while the planet is off the limb of the star as well. We set θ to the first zero of the the phase function, $P(\theta)$ (Equation 5), and solved to obtain the critical particle size, a_{crit} , which we define to be the ring particle radius near which diffraction’s effect on the lightcurve is maximized, using the small angle approximation:

$$a_{crit} = .61 \times \frac{a_p \lambda}{R_*} \quad (10)$$

Transit lightcurves for ringed planets change significantly as a varies within an order of magnitude of a_{crit} . However for particle diameters $a \gtrsim 10 \times a_{crit}$ and $a \lesssim a_{crit}/10$, transit lightcurves are indistinguishable from those for $a = 10 \times a_{crit}$ and for $a = a_{crit}/10$ respectively. Thus large particles are those with $a \gg a_{crit}$, and small particles are those with $a \ll a_{crit}$.

Parcels of ring containing particles with diameters within a factor of ~ 10 of a_{crit} scatter light to the observer both before and after they encounter the stellar limb, as viewed from Earth. This leads to an increased photometric flux measured just before first contact, and just after fourth contact during a transit event. The lightcurve signature (see Figure 6, inset) of this ramp is diagnostic of diffractive scattering. Moreover, the characteristic size of the extrasolar planet ring particles can be determined from the shape and magnitude of the pre- and post-transit scattering signature.

Only if the ring particle diameters are within a factor of 10 of a_{crit} can anything at all be discerned about the particle sizes – otherwise, lightcurve models using very large particles and those using very small particles will fit equally well.

Similar lightcurve ramps to the ones shown in Figure 6

can result from refraction through the outer layers of the atmosphere of a transiting extrasolar giant planet. Hubbard et al. (2001) showed that refractive scattering will likely become important only for planets with semimajor axes of tens of AU or greater. In particular, our calculations (using the codes developed for Hubbard et al. (2001)) show that the refraction ramp for a typical transiting EGP at 14 AU would be 100 times smaller than the ring diffraction ramps in Figure 6. Therefore, a detected lightcurve ramp for a transiting ringed planet can reasonably be ascribed to diffraction from ring particles.

Near a_{crit} , rings’ diffractive scattering affects the planet’s transit lightcurve in between first and fourth contacts as well. As shown in Figure 6, the depth of the transit bottom decreases as ring particle size increases because inside the transit larger particles scatter light incident upon the ring into the direction of the observer more efficiently than small particles do. If $a \sim a_{\text{crit}}$, more of the diffraction footprint will overlap with the star near mid-transit than at the beginning and end of transit. In this case, more diffracted light is detected at midtransit, and the transit lightcurve bottom is flattened. Fitting the simulated lightcurves plotted in Figure 6 with spherical planets, we calculate that the flattening is of order $\Delta c_1 \sim 0.1$ for a standard ring.

Though the lightcurve deviations described in this section are illustrative of those we would expect to see owing to diffraction through planetary rings, they are not a perfect calculation of what diffraction through a real ring system will look like. An actual ring system is likely to have complexity in its radial structure that we have not simulated here. Also, real ring particles will have a nonuniform distribution of sizes, similar to the particles that make up Saturn’s rings (French & Nicholson 2000). We are able to say, however, that diffraction around appropriately sized ring particles can lead to a ramp in the transit lightcurve of a ringed extrasolar planet, that this ramp can be detectable, and that such a ramp is greatly in excess of the expected magnitude for similar ramps resulting from planetary atmospheric effects.

5. APPLICATION

Saturn’s ring system is distinctly more complex than the $\tau = 1, 1.5 - 2.0R_{Jup}$ standard ring that we have used up to this point. In particular, Dyudina et al. (2003) showed that the intricate radial optical depth structure of Saturn’s rings significantly alters the directly-detected orbital lightcurve relative to the lightcurve for radially uniform rings.

To test whether the detectability of complex ring systems differs substantially from that of our simple standard ring, we used a radial optical depth profile of Saturn’s rings obtained during the 28 Sgr occultation in 1989 (French & Nicholson 2003) binned down into 39 subrings. We set the rings’ particle diameter to 1 cm, a typical value from French & Nicholson (2000). We then simulated transits of Saturn at impact parameter 0.2, calculated a best-fit spherical planet transit to match, and subtracted the two

to represent Saturn’s detectability.

The detectability of the rings around Saturn, as shown in Figure 8, is a bit less than the standard ring because the total area covered is smaller. However, the character of the ring signal is the same as that of the standard ring. Extrasolar astronomers, viewing a transit of Saturn with a photometric precision of 10^{-4} from 28 Sgr, would detect Saturn’s rings as long as the axis angle ϕ wasn’t such that they were viewed edge-on.

At 10 AU from the Sun, a_{crit} for Saturn is 0.66 mm (from Equation 10). Therefore, as calculated Saturn’s particle size falls in the large regime and we would predict no scattering effects to be discernable. Figure 8 does not show any significant pre- or post-transit scattered light, in agreement with our analysis. Without a positive identification of scattering, the astronomers from 28 Sgr would not know whether the ring particles were large or small, and therefore would not know whether their measured ring optical depth corresponded to the geometric optical depth (τ_g) or the total optical depth (τ – see Section 4.2).

6. CONCLUSION

The primary effect rings have on a planet’s transit lightcurve is to increase the transit depth. Without knowledge of the rings’ existence, the best-fit unadorned spherical model planet will have an anomalously large radius and transit closer to $b = 0.7$ than the actual ringed planet.

The detection of large, Saturn-like ring systems requires photometric precision of a few $\times 10^{-4}$, achievable with space based photometers and potentially from future ground-based platforms. The transit signature of rings is concentrated at ingress and egress, and therefore ring detection requires high time-resolution photometry.

Diffraction around individual ring particles manifests as forward scattering that can be detected from transit lightcurves as excess flux just before and just after a ringed planet’s transit. The shape and magnitude of the scattering signal can be used to discern the ring particles’ modal diameter.

The frequency and distribution of rings around planets at different semimajor axes, of different ages, and with different insolarations can empirically determine how rings form and how long they last.

In the near-future, the experiments described in this paper can be tested on close-in transiting planets found from the ground, using follow-up transit photometry from space. Later, the NASA Discovery mission *Kepler* will be capable of both detecting planets with larger semimajor axes, and surveying these new worlds for rings. Together, these observations hold the promise to establish a rough outline of the distribution of large Saturn-like ring systems within the next decade.

The authors wish to thank: Robert H. Brown and

William B. Hubbard for excellent advising; Renu Malhotra, Gwen Bart, and Wayne Barnes for manuscript suggestions; and Peter Lanagan for allowing the generous use of his U of A Press library.

REFERENCES

- Arnold, L. & Schneider, J. 2004, *A&A*, 420, 1153
- Barnes, J. W. & Fortney, J. J. 2003, *ApJ*, 588, 545
- Barnes, J. W. & O'Brien, D. P. 2002, *ApJ*, 575, 1087
- Bodenheimer, P., Laughlin, G., & Lin, D. N. C. 2003, *ApJ*, 592, 555
- Bouchy, F., Pont, F., Santos, N. C., Melo, C., Mayor, M., Queloz, D., & Udry, S. 2004, *A&A*, 421, L13
- Brown, T. M., Charbonneau, D., Gilliland, R. L., Noyes, R. W., & Burrows, A. 2001, *ApJ*, 552, 699
- Charbonneau, D., Brown, T. M., Latham, D. W., & Mayor, M. 2000, *ApJ*, 529, L45
- Charbonneau, D., Brown, T. M., Noyes, R. W., & Gilliland, R. L. 2002, *ApJ*, 568, 377
- Charbonneau, D., Noyes, R. W., Korzennik, S. G., Nisenson, P., Jha, S., Vogt, S. S., & Kibrick, R. I. 1999, *ApJ*, 522, L145
- Collier Cameron, A., Horne, K., James, D., Penny, A., & Semel, M. 2000, *ArXiv Astrophysics e-prints*
- Collier Cameron, A., Horne, K., Penny, A., & Leigh, C. 2002, *MNRAS*, 330, 187
- Cuzzi, J. N. 1985, *Icarus*, 63, 312
- Dyudina, U. A., Del Genio, A. D., Dones, L., Throop, H. B., Porco, C. C., & Seager, S. 2003, *AAS/Division for Planetary Sciences Meeting*, 35, 0
- Ferrari, C. & Brahic, A. 1994, *Icarus*, 111, 193
- French, R. & Nicholson, P. 2003, *NASA Planetary Data System*, USA_NASA_PDS_EBROCC_001
- French, R. G. & Nicholson, P. D. 2000, *Icarus*, 145, 502
- Galilei, G. 1989, *Sidereus nuncius, or, The Sidereal messenger* (Chicago : University of Chicago Press, 1989.)
- Gaudi, B. S., Chang, H., & Han, C. 2003, *ApJ*, 586, 527
- Hecht, E. 1998, *Optics* (Reading, MA: Addison-Wesley)
- Henry, G. W., Marcy, G. W., Butler, R. P., & Vogt, S. S. 2000, *ApJ*, 529, L41
- Horne, K. 2003, *ArXiv Astrophysics e-prints*
- Howell, S. B., Everett, M. E., Tonry, J. L., Pickles, A., & Dain, C. 2003, *PASP*, 0, 000
- Hubbard, W. B., Fortney, J. J., Lunine, J. I., Burrows, A., Sudarsky, D., & Pinto, P. 2001, *ApJ*, 560, 413
- Jenkins, J. M. & Doyle, L. R. 2003, *ArXiv Astrophysics e-prints*
- Karkoschka, E. 2001, *Icarus*, 151, 78

Konacki, M., Torres, G., Jha, S., & Sassellov, D. 2003, Nature

Konacki, M., Torres, G., Sassellov, D. D., Pietrzyński, G., Udalski, A., Jha, S., Ruiz, M. T., Gieren, W., & Minniti, D. 2004, ApJ, 609, L37

Press, W. H., Teukolsky, S. A., Vetterling, W. T., & Flannery, B. P. 1992, Numerical recipes in C. The art of scientific computing (Cambridge: University Press)

Sartoretti, P. & Schneider, J. 1999, A&AS, 134, 553

Vidal-Madjar, A., Lecavelier des Etangs, A., Désert, J.-M., Ballester, G. E., Ferlet, R., Hébrard, G., & Mayor, M. 2003, Nature, 422, 143

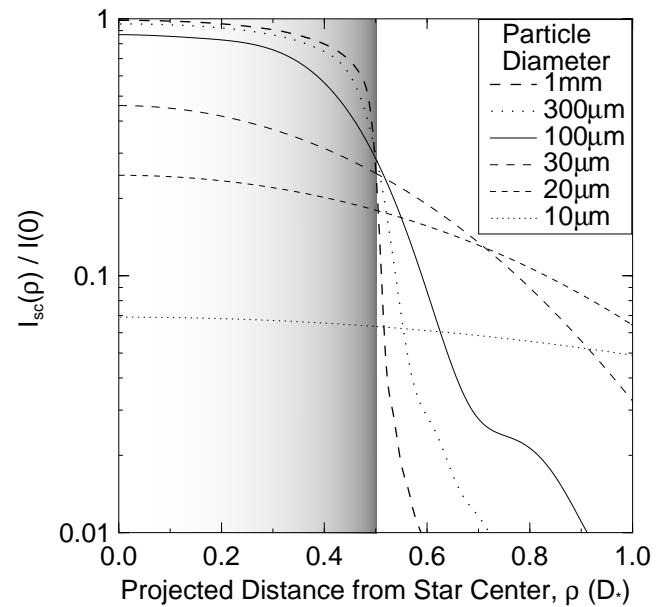


Fig. 5.— Here we graph the scattering efficiency calculated in the same way as it was for Figure 4, but do so in a different way, as a function of projected distance from the star center and for different particle diameters. The shading in the background represents the actual limb darkened stellar flux.

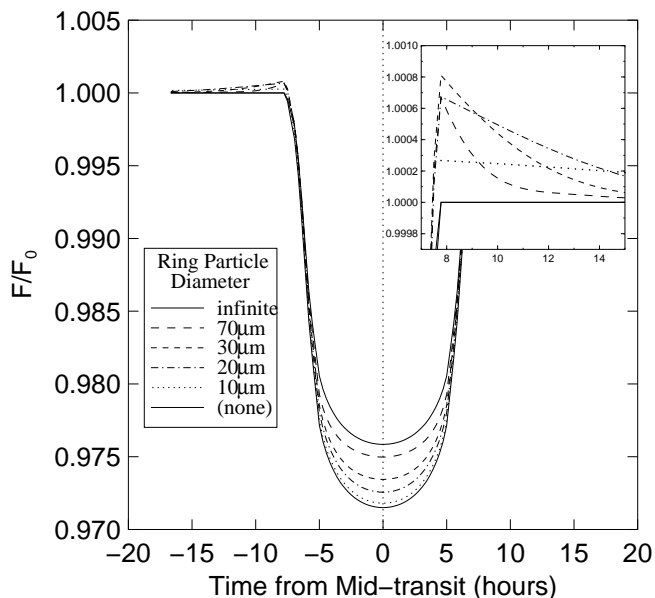


Fig. 6.— Here we show the changes introduced into a transit lightcurve when diffractive forward scattering is incorporated into the calculation. This figure shows transit lightcurves at $0.5\mu\text{m}$ for a $1 R_J$ planet with a $1.5 R_J$ to $2.0 R_J$ optical depth unity ring composed of particles of varying sizes. The planet orbits its $1 R_\odot$, $c_1 = 0.64$ star at 1 AU, and transits with an impact parameter of 0.2. The bottom solid line represents what the lightcurve calculated with extinction only – no scattering. The rest of the curves do incorporate scattering along with extinction, and do so for differing particle diameters: $10\mu\text{m}$ (dotted line), $20\mu\text{m}$ (dash-dotted line), $30\mu\text{m}$ (short-dashed line), $70\mu\text{m}$ (long-dashed line), and the theoretical (though meaningless in practice) limit of infinite particle size (top solid line).

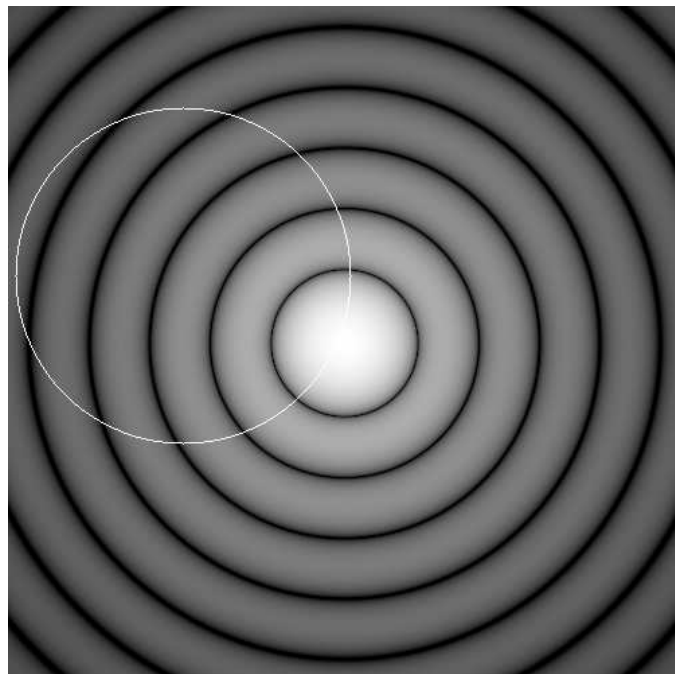


Fig. 7.— This image represents the diffraction footprint of a hypothetical cloud of $150\mu\text{m}$ particles (located at the center of the image) 1 AU from a $1 R_\odot$ star (the star's limb is depicted as a white circle) as it would look at $0.5\mu\text{m}$. The intensity of each pixel represents the logarithm of the relative contribution of light that diffraction scatters toward the observer from each area. The area directly behind the particles contributes most of the diffracted light. The effect of diffraction on a ringed planet's transit lightcurve is most detectable when the radius of the first dark fringe is $\sim 1R_*$. Since this process is reversible, the same pattern would result if you fired a laser toward the cloud of particles from Earth and then, hundreds of years later, viewed the resulting diffraction pattern on a gigantic screen millions of km across centered on the position of the star. In practice, because of the nonuniform radii and shape of the ring particles such a sharp pattern would never actually occur.

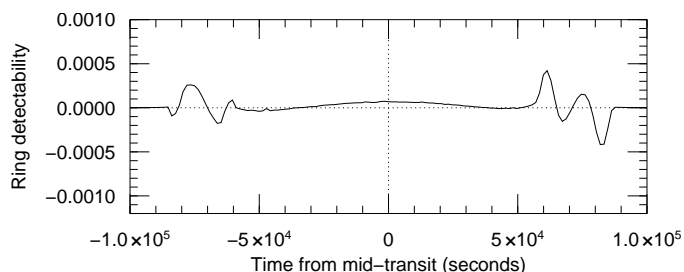


Fig. 8.— Predicted transit detectability of Saturn's rings, as might be viewed from 28 Sgr. The magnitude is lower than that for the standard ring owing to the smaller cross-sectional area of Saturn's rings, but the character of the signal is the same. No scattering is evident, so Saturn's ring particle size would not be discernable.